Biomedical Optics EXPRESS

Development of a high power supercontinuum source in the 1.7 μm wavelength region for highly penetrative ultrahigh-resolution optical coherence tomography

H. Kawagoe,[1,*] S. Ishida,[1] M. Aramaki,[1] Y. Sakakibara,[2,3] E. Omoda,[2] H. Kataura,[2,3] and N. Nishizawa[1]

[1] *Dept. Electrical Engineering and Computer Science, Nagoya University, Furo-cho, Chikusa-ku, Nagoya 464-8603, Japan*

[2] *National Institute of Advanced Industrial Science and Technology (AIST), Tsukuba 305-8565, Japan*

[3] *JST, CREST, Kawaguchi, Saitama 330-0012, Japan*

[*] *kawagoe.hiroyuki@e.mbox.nagoya-u.ac.jp*

Abstract: We developed a high power supercontinuum source at a center wavelength of 1.7 μm to demonstrate highly penetrative ultrahigh-resolution optical coherence tomography (UHR-OCT). A single-wall carbon nanotube dispersed in polyimide film was used as a transparent saturable absorber in the cavity configuration and a high-repetition-rate ultrashort-pulse fiber laser was realized. The developed SC source had an output power of 60 mW, a bandwidth of 242 nm full-width at half maximum, and a repetition rate of 110 MHz. The average power and repetition rate were approximately twice as large as those of our previous SC source [20]. Using the developed SC source, UHR-OCT imaging was demonstrated. A sensitivity of 105 dB and an axial resolution of 3.2 μm in biological tissue were achieved. We compared the UHR-OCT images of some biological tissue samples measured with the developed SC source, the previous one, and one operating in the 1.3 μm wavelength region. We confirmed that the developed SC source had improved sensitivity and penetration depth for low-water-absorption samples.

OCIS codes: (110.4500) Optical coherence tomography; (170.3880) Medical and biological imaging.

References and links

1. D. Huang, E. A. Swanson, C. P. Lin, J. S. Schuman, W. G. Stinson, W. Chang, M. R. Hee, T. Flotte, K. Gregory, C. A. Puliafito, and J. G. Fujimoto, "Optical coherence tomography," Science **254**(5035), 1178–1181 (1991).
2. J. M. Schmitt, "Optical coherence tomography (OCT): a review," IEEE J. Sel. Top. Quantum Electron. **5**(4), 1205–1215 (1999).
3. A. M. Zysk, F. T. Nguyen, A. L. Oldenburg, D. L. Marks, and S. A. Boppart, "Optical coherence tomography: a review of clinical development from bench to bedside," J. Biomed. Opt. **12**(5), 051403 (2007).
4. R. A. Costa, M. Skaf, L. A. S. Melo, Jr., D. Calucci, J. A. Cardillo, J. C. Castro, D. Huang, and M. Wojtkowski, "Retinal assessment using optical coherence tomography," Prog. Retin. Eye Res. **25**(3), 325–353 (2006).
5. M. Mujat, R. C. Chan, B. Cense, B. H. Park, C. Joo, T. Akkin, T. C. Chen, and J. F. de Boer, "Retinal nerve fiber layer thickness map determined from optical coherence tomography images," Opt. Express **13**(23), 9480–9491 (2005).
6. M. Nishiura, T. Kobayashi, M. Adachi, J. Nakanishi, T. Ueno, Y. Ito, and N. Nishizawa, "In vivo ultrahigh-resolution ophthalmic optical coherence tomography using gaussian-shaped supercontinuum," Jpn. J. Appl. Phys. **49**(1), 012701 (2010).
7. B. W. Colston, Jr., M. J. Everett, L. B. Da Silva, L. L. Otis, P. Stroeve, and H. Nathel, "Imaging of hard- and soft-tissue structure in the oral cavity by optical coherence tomography," Appl. Opt. **37**(16), 3582–3585 (1998).

#203700 - $15.00 USD Received 24 Dec 2013; revised 15 Feb 2014; accepted 18 Feb 2014; published 26 Feb 2014

8. L. L. Otis, B. W. Colston, Jr., M. J. Everett, and H. Nathel, "Dental optical coherence tomography: a comparison of two in vitro systems," Dentomaxillofac. Radiol. **29**(2), 85–89 (2000).
9. A. Z. Freitas, D. M. Zezell, N. D. Vieira, A. C. Ribeiro, and A. S. L. Gomes, "Imaging carious human dental tissue with optical coherence tomography," J. Appl. Phys. **99**(2), 024906 (2006).
10. G. Isenberg and M. V. Sivak, Jr., "Gastrointestinal optical coherence tomography," Tech. Gastrointest. Endosc. **5**(2), 94–101 (2003).
11. M. C. Pierce, J. Strasswimmer, B. H. Park, B. Cense, and J. F. de Boer, "Advances in optical coherence tomography imaging for dermatology," J. Invest. Dermatol. **123**(3), 458–463 (2004).
12. M. J. Yadlowsky, J. M. Schmitt, and R. F. Bonner, "Multiple scattering in optical coherence microscopy," Appl. Opt. **34**(25), 5699–5707 (1995).
13. J. M. Schmitt, A. Knüttel, M. Yadlowsky, and M. A. Eckhaus, "Optical-coherence tomography of a dense tissue: statistics of attenuation and backscattering," Phys. Med. Biol. **39**(10), 1705–1720 (1994).
14. Y. Pan and D. L. Farkas, "Noninvasive imaging of living human skin with dual-wavelength optical coherence tomography in two and three dimensions," J. Biomed. Opt. **3**(4), 446–455 (1998).
15. S. Radhakrishnan, A. M. Rollins, J. E. Roth, S. Yazdanfar, V. Westphal, D. S. Bardenstein, and J. A. Izatt, "Real-time optical coherence tomography of the anterior segment at 1310 nm," Arch. Ophthalmol. **119**(8), 1179–1185 (2001).
16. A. Aguirre, N. Nishizawa, J. G. Fujimoto, W. Seitz, M. Lederer, and D. Kopf, "Continuum generation in a novel photonic crystal fiber for ultrahigh resolution optical coherence tomography at 800 nm and 1300 nm," Opt. Express **14**(3), 1145–1160 (2006).
17. B. E. Bouma, L. E. Nelson, G. J. Tearney, D. J. Jones, M. E. Brezinski, and J. G. Fujimoto, "Optical coherence tomographic imaging of human tissue at 1.55 μm and 1.81 μm using Er- and Tm-doped fiber sources," J. Biomed. Opt. **3**(1), 76–79 (1998).
18. N. Nishizawa, Y. Chen, P. Hsiung, E. P. Ippen, and J. G. Fujimoto, "Real-time, ultrahigh-resolution, optical coherence tomography with an all-fiber, femtosecond fiber laser continuum at 1.5 microm," Opt. Lett. **29**(24), 2846–2848 (2004).
19. U. Sharma, E. W. Chang, and S. H. Yun, "Long-wavelength optical coherence tomography at 1.7 microm for enhanced imaging depth," Opt. Express **16**(24), 19712–19723 (2008).
20. S. Ishida, N. Nishizawa, T. Ohta, and K. Itoh, "Ultrahigh-resolution optical coherence tomography in 1.7 μm region with fiber laser supercontinuum in low-water-absorption samples," Appl. Phys. Express **4**(5), 052501 (2011).
21. S. Ishida and N. Nishizawa, "Quantitative comparison of contrast and imaging depth of ultrahigh-resolution optical coherence tomography images in 800-1700 nm wavelength region," Biomed. Opt. Express **3**(2), 282–294 (2012).
22. V. M. Kodach, J. Kalkman, D. J. Faber, and T. G. van Leeuwen, "Quantitative comparison of the OCT imaging depth at 1300 nm and 1600 nm," Biomed. Opt. Express **1**(1), 176–185 (2010).
23. N. Nishizawa, Y. Seno, K. Sumimura, Y. Sakakibara, E. Itoga, H. Kataura, and K. Itoh, "All-polarization-maintaining Er-doped ultrashort-pulse fiber laser using carbon nanotube saturable absorber," Opt. Express **16**(13), 9429–9435 (2008).
24. Y. Senoo, N. Nishizawa, Y. Sakakibara, K. Sumimura, E. Itoga, H. Kataura, and K. Itoh, "Polarization-maintaining, high-energy, wavelength-tunable, Er-doped ultrashort pulse fiber laser using carbon-nanotube polyimide film," Opt. Express **17**(22), 20233–20241 (2009).
25. F. M. Mitschke and L. F. Mollenauer, "Discovery of the soliton self-frequency shift," Opt. Lett. **11**(10), 659–661 (1986).
26. N. Nishizawa and T. Goto, "Compact System of Wavelength-Tunable Femtosecond Soliton Pulse Generation Using Optical Fibers," IEEE Photon. Technol. Lett. **11**(3), 325–327 (1999).
27. N. Nishizawa and J. Takayanagi, "Octave spanning high-quality supercontinuum generation in all fiber system," J. Opt. Soc. Am. B **24**(8), 1786 (2007).

1. Introduction

Optical coherence tomography (OCT) is a non-invasive optical imaging technique used for micrometer-scale cross-sectional imaging of biological tissue and materials [1–3]. It is an essential imaging technique in ophthalmology, and has also been studied recently in various other clinical, industrial, and research applications [4–11]. For such applications, it is necessary to increase both the penetration depth and resolution. An axial resolution of less than 5 μm can be achieved by using a broad spectral light source such as superluminescent diodes (SLDs), ultrashort pulse solid state lasers, and supercontinuum (SC) sources. However, the average output power of SLDs is limited to a few tens of mW, and the spectral shape is not ideal and it needs shaping to achieve the ideal interference signal. For the ultrashort pulse solid state lasers, the environmental stability is weak. The optical spectrum cannot be controlled and the available wavelength is limited by the laser source. For the SC

#203700 - $15.00 USD Received 24 Dec 2013; revised 15 Feb 2014; accepted 18 Feb 2014; published 26 Feb 2014

sources, we can demonstrate high power, wideband light source at various wavelength regions.

The penetration depth of OCT is fundamentally limited by the attenuation of ballistic light propagation via scattering and absorption. Besides the scattering and absorption losses, the phenomenon of multiple scattering also makes it difficult to achieve meaningful structural information at deeper penetration depths [12]. Because the optical properties of tissue have a strong dependence on wavelength, it is necessary to choose the proper wavelength to achieve a large penetration depth. A clear improvement in penetration depth was demonstrated by using a wavelength of 1.3 μm versus 0.8 μm [7,13–16]. OCT systems operating at 1.55 μm and 1.8 μm have shown comparable penetration depths to that of 1.3 μm systems [17,18]. Recently, OCT systems operating in long-wavelength regions at 1.7 μm and at 1.3 μm were compared for imaging skin, 10% intralipid solution, and rubber [19]. Ishida *et al.* demonstrated highly penetrative UHR-OCT imaging for the first time by using a fiber-based Gaussian-like SC at a center wavelength of 1.7 μm and confirmed the wavelength dependence of the imaging contrast and penetration depth in the 0.8–1.7 μm wavelength region [20–22]. Increased penetration depth was achieved due to lower scattering in tissue at longer wavelengths. In OCT, the sensitivity is proportional to the signal power. Thus, for highly sensitive measurement, it is important to increase the average power of the SC. In those systems, however, the power of the SC in the 1.7 μm wavelength region was inhibited by large nonlinear effects in fibers. As a result, both the sensitivity and the penetration depth of OCT were limited by the allowable power of the SC. In order to perform OCT imaging with higher sensitivity and deeper penetration, it is important to increase the output power of the SC source in the 1.7 μm wavelength region. Moreover, especially in clinical applications, the optical sources must have very high robustness against disturbances, as well as both short- and long-term stability. Therefore, an almost entirely all-fiber configuration is desirable for the SC source.

In this study, we developed a high-power SC source to demonstrate highly penetrative UHR-OCT in the 1.7 μm wavelength region. We constructed a high-power SC source with a center wavelength of 1.7 μm based on a high-repetition-rate ultrashort-pulse fiber laser using single-wall carbon nanotubes (SWNTs) [23,24]. We compared the imaging contrast and penetration depth of UHR-OCT images obtained using the SC source developed in the present study, a previously developed one, and an SC source operating in the 1.3 μm wavelength region. The developed high-power system showed improved imaging contrast and penetration depth.

2. Experimental setup

2.1. High-power supercontinuum source operating in 1.7 μm wavelength region

We constructed a high-power SC source operating in the 1.7 μm wavelength region. For the seed pulse of the SC, we built a high-repetition-rate mode-locked ultrashort-pulse fiber laser using SWNTs. Figure 1 shows a schematic diagram. The fiber laser was composed of fiber-based components and a polyimide film in which SWNTs were dispersed [23,24]. We used SWNTs synthesized with the high-pressure CO (HiPco) method. The linear absorption coefficient of the SWNTs was 40% and the modulation depth was 10%. The polyimide film was easily inserted between a pair of FC/APC fiber connectors, so that there was no need for a spatial optical alignment system. A high-concentration Er-doped fiber (EDF) exhibiting anomalous-dispersion properties (LIEKKI, Er80-8/125) was used as a gain medium. The total cavity length of the fiber laser was shortened to about 1.8 m, and a high repetition rate of 110 MHz was achieved. This was approximately twice as high as that of our previous SC source with a 47 MHz repetition rate [20].

#203700 - $15.00 USD Received 24 Dec 2013; revised 15 Feb 2014; accepted 18 Feb 2014; published 26 Feb 2014

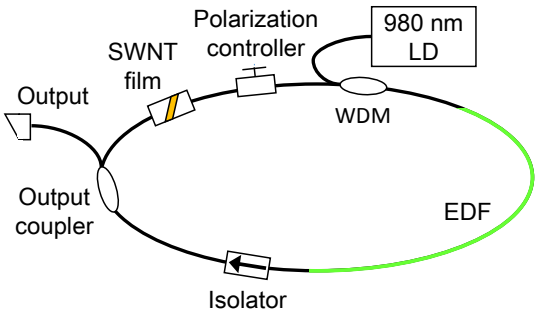

Fig. 1. Experimental setup of the developed high repetition rate ultrashort pulse fiber laser using SWNT. EDF, Er-doped fiber; WDM, wavelength division multiplexed coupler.

Figure 2(a) shows the output power as a function of the pump power. As the pump power was increased, the output power increased linearly, and the oscillation mode shifted from cw lasing to self-Q switching, and then to single-pulse soliton mode-locking operation. The maximum output power was about 40 mW, which, to our knowledge, is the highest reported average power for single-pulse soliton mode-locking operation in SWNT fiber lasers. Figure 2(b) shows the spectral and temporal widths, full-width at half-maximum (FWHM), as a function of the pump power. As the pump power was increased, the spectral width increased and the temporal width decreased monotonically.

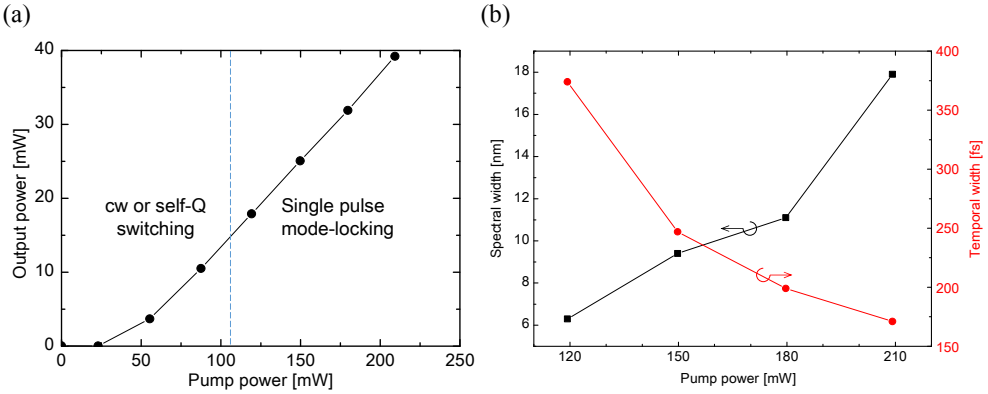

Fig. 2. Variations of (a) the output power and the operation mode, and (b) spectral and temporal widths as a function of the pump power.

Figure 3 shows the optical characteristics of the output ultrashort pulse when the pump power was 210 mW. As shown in Fig. 3(a), the maximum spectral width was 18 nm FWHM. The observed temporal width of the autocorrelation trace was 265 fs, and the corresponding temporal width was 171 fs under the assumption of a sech^2 pulse shape. From numerical analysis of the pulse dynamics inside the cavity, we confirmed that, owing to the soliton compression, the pulse width obtained at the output of the fiber laser was almost the shortest one which can be obtained in this laser.

#203700 - $15.00 USD Received 24 Dec 2013; revised 15 Feb 2014; accepted 18 Feb 2014; published 26 Feb 2014

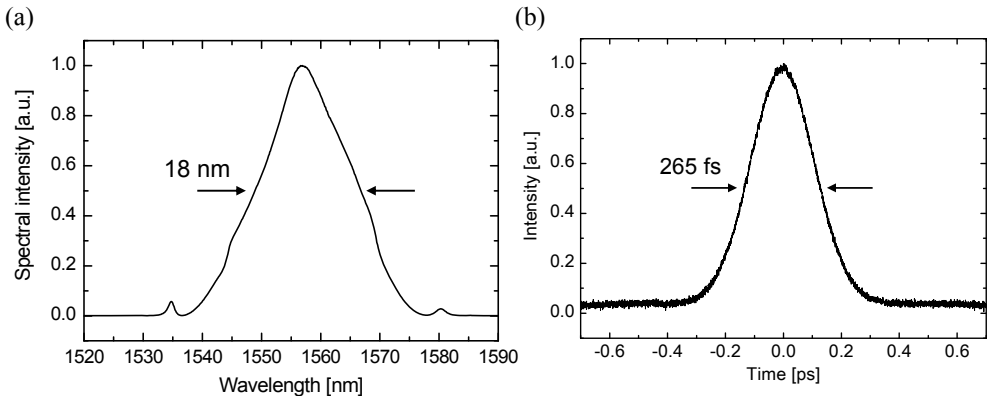

Fig. 3. Characteristics of the output pulse of the fiber laser, (a) the optical spectrum and (b) the autocorrelation trace.

Next, we examined the RF noise of the fiber laser. Figure 4(a) shows the result of single-sideband measurement, which is generally used for amplitude noise measurement of mode-locked laser sources. There was no large intensity noise component. Figure 4(b) shows the observed RF spectra of the output pulse train. We used a 30 dB neutral density (ND) filter to avoid saturation of the RF spectrum analyzer. The black line shows the RF spectrum of the output pulse train, and the red line shows the detection system noise measured without a signal. Equally spanned, clean RF spectra were observed. These results indicated stable mode-locking operation, and we confirmed that the developed high-repetition-rate fiber laser had low noise.

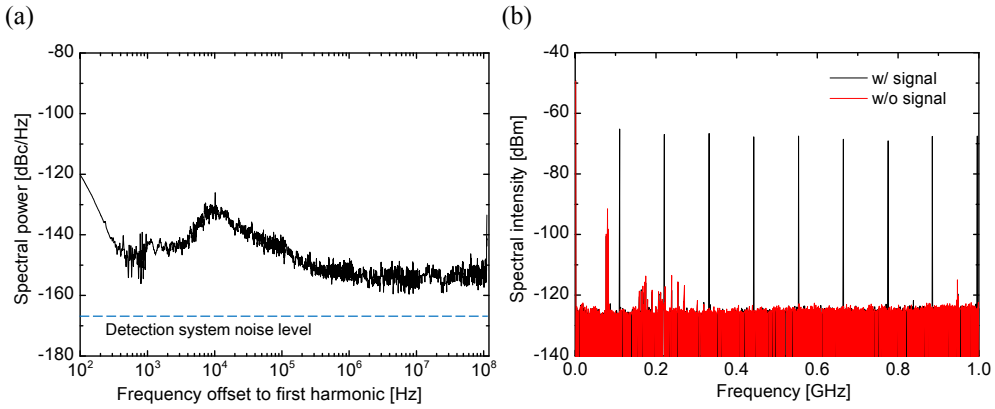

Fig. 4. Observed RF spectra for (a) single sideband measurement and (b) 0-1.0 GHz region of the developed high repetition rate fiber laser.

Figure 5 shows the scheme of the developed high-power SC source in the 1.7 μm wavelength region based on the SWNT fiber laser. The Er-doped fiber amplifier system (EDFA) consisted of a high-Er-concentration EDF with normal-dispersion properties (LIEKKI, Er110-4/125) pumped by three high power laser diodes operating at 1480 nm (Furukawa Electric Co., Ltd.,). The output of the SWNT fiber laser was passed through a variable attenuator, which was constructed of two half-wave plates, a quarter-wave plate, and a polarization beam splitter, in order to avoid pulse breaking in the EDFA. After the EDFA, the amplified pulse was coupled into a polarization maintaining fiber (PMF). In the PMF, the amplified pulse was broken up into two pulses, and a new optical pulse was generated at the longer wavelength side of the amplified pulse due to Raman scattering. In the pulse

#203700 - $15.00 USD Received 24 Dec 2013; revised 15 Feb 2014; accepted 18 Feb 2014; published 26 Feb 2014

propagation, the generated pulse formed the fundamental soliton pulse due to the interaction between group-velocity dispersion and self-phase modulation (SPM). Owing to the intra-pulse Raman scattering, the shorter wavelength components were converted into longer wavelength ones, and the center wavelength of the soliton pulse was shifted toward the longer wavelength side [25,26]. Accordingly, a Raman soliton pulse was generated in the 1.7 μm wavelength region. The average output power and the pulse energy of the Raman soliton pulse were about 120 mW and 1.09 nJ, respectively. The center wavelength and the spectral width were 1671 nm and 21.4 nm, respectively. Based on the time–bandwidth product of a transform-limited sech^2 pulse, the temporal width of the Raman soliton pulse was estimated to be about 137 fs, and therefore, the peak power of the Raman soliton pulse was estimated to be 8.0 kW. This was slightly low compared with that of the previous one [20]. After eliminating residual components in the shorter wavelength region by using a low pass filter, the Raman soliton pulse was coupled into the prototype model of a highly nonlinear fiber (HNLF) with normal dispersion [27]. The dispersion parameters β_2 and β_3 of this HNLF were 6.37 ps^2 km^{-1} and −0.0057 ps^3 km^{-1} at a wavelength of 1.56 μm, respectively, and the magnitudes of β_2 and β_3 were small in the 1.3–1.8 μm spectral region. The nonlinear coefficient was 23 W^{-1} km^{-1} at 1.56 μm. In this HNLF, SPM was induced by the Raman soliton pulse. Owing to the effects of SPM, the normal dispersion properties, and the ideal sech^2 shape of the soliton pulse, a high-power and smoothly broadened SC was generated at a center wavelength of 1.7 μm [27]. The maximum output power of the developed SC was 60 mW, which was twice as large as that of the previous one [20].

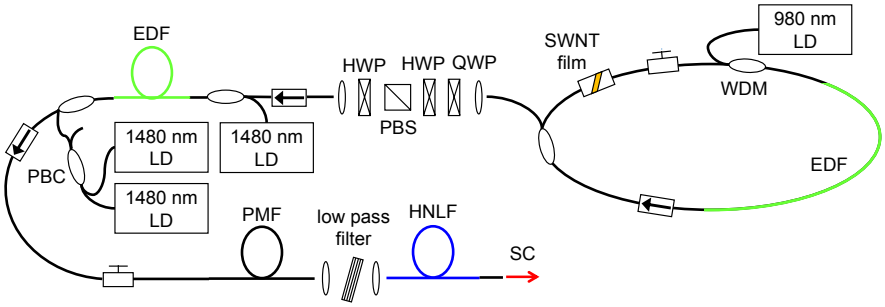

Fig. 5. Experimental setup of 1.7 μm high power SC source. QWP, quarter-wave plate; HWP, half-wave plate; PBS, polarization beam splitter; PBC, polarization beam combiner; PMF, polarization maintaining fiber; HNLF, highly nonlinear fiber.

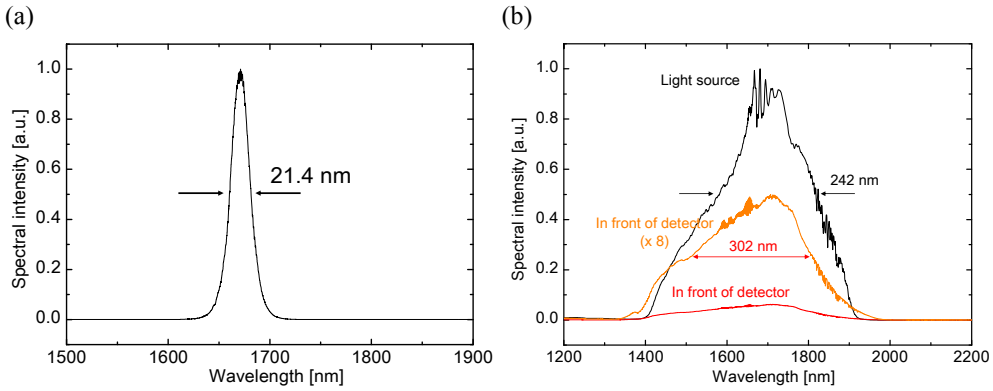

Fig. 6. Optical spectra of (a) the Raman soliton pulse and (b) the high power SC (black line, light source; red one, in front of detector; orange one, in front of detector (enlarged).).

#203700 - $15.00 USD Received 24 Dec 2013; revised 15 Feb 2014; accepted 18 Feb 2014; published 26 Feb 2014

Figure 6 shows the obtained optical spectra of the Raman soliton pulse and the generated SC. The spectral width of the generated SC was 242 nm FWHM, and the corresponding theoretical axial resolution was 5.3 μm in air. Using the high-repetition-rate SWNT fiber laser, excessive nonlinear effects were suppressed, allowing a Gaussian-shaped SC to be generated.

Typically, the commercially available SC source is generated with nsec-psec pulses and the dispersion shifted highly nonlinear fibers. However, the noise level of those SC is generally higher than that of SLD by 20-30 dB. On the other hand, using the fs ultrashort pulse and normal dispersion highly nonlinear fiber, a Gaussian-like shaped, wideband SC with low-noise property can be realized [27].

This system consisted almost entirely of all-fiber components and can fit inside a shoe box. The developed SC source showed good long-term stability for 24 hours. The spectral noise was negligibly small during the imaging. Therefore, this light source can be used as a compact, stable, and practical wideband source for OCT.

2.2 UHR-OCT system

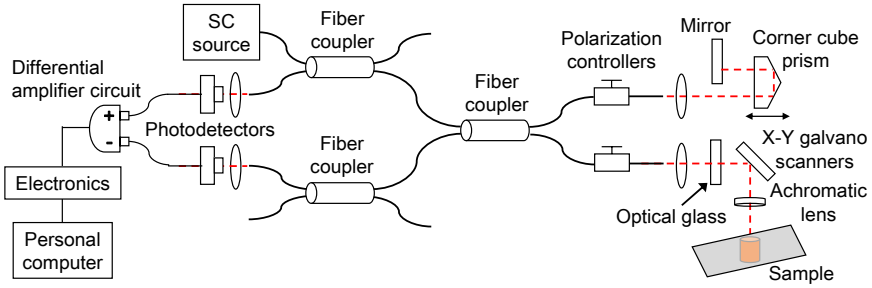

Fig. 7. Experimental setup of the ultrahigh resolution OCT system operating at 1.7 μm wavelength.

At this stage, since the line scan camera which covers the longer wavelength region was not available, it was difficult to demonstrate spectral domain OCT. So we constructed a time-domain OCT (TD-OCT) system. As illustrated in Fig. 7, the system was based on a Michelson interferometer composed of three broadband fiber couplers. We employed three optical fiber couplers to use the balanced detection system. The optical path length of the reference beam was scanned using a corner cube prism mounted on a galvanometer. The A-line scan rate was 100 Hz which is determined by the scanning speed of the corner cube prism, and the B-scan rate was about 0.14 Hz. The signal beam was spatially scanned using an X-Y galvanometer-based scanning probe, and automated imaging was performed. For highly sensitive measurement, we used an InGaAs detector with extended wideband characteristics in the 1.2–2.6 μm wavelength region (Thorlabs, PDA10D). A balanced detection configuration with two extended InGaAs detectors was used to cancel out the average noise. In addition, optical glasses were employed to compensate for the difference in chromatic dispersion between the reference and sample arms, and polarization controllers matched the polarization state of light in the two arms in order to achieve ultrahigh-resolution imaging. For the measurement of the interference signal, a mirror was used in the sample arm. In order to avoid saturation, a 20 dB ND filter was inserted in the sample arm (not shown in Fig. 7), so that the interference signal was attenuated by 40 dB in total. Figure 8(a) shows the interference signal measured by the UHR-OCT system with the developed SC source. The side lobe level was very low owing to the Gaussian-shaped spectrum. The axial resolution was 4.4 μm in air, corresponding to 3.2 μm in biological tissue with a refractive index of 1.38. It's interesting to note that the observed axial resolution was higher than that of the theoretical axial resolution estimated from the light source. It was experimentally confirmed that the FWHM bandwidth of the optical spectra in front of the detector was

#203700 - $15.00 USD Received 24 Dec 2013; revised 15 Feb 2014; accepted 18 Feb 2014; published 26 Feb 2014

increased by the spectral shaping caused by the wavelength dependence in the fiber couplers, as shown in Fig. 6(b). Figure 8(b) shows the logarithmically demodulated signal observed with the ND filter. The system sensitivity was 105 dB. This was 10 dB larger than that of the previous SC source [20]. With the use of broadband optical circulators a higher sensitivity may be achieved. The lateral resolution of the sample surface was about 33 μm. The confocal parameter was 1.01 mm (twice the Rayleigh range in air).

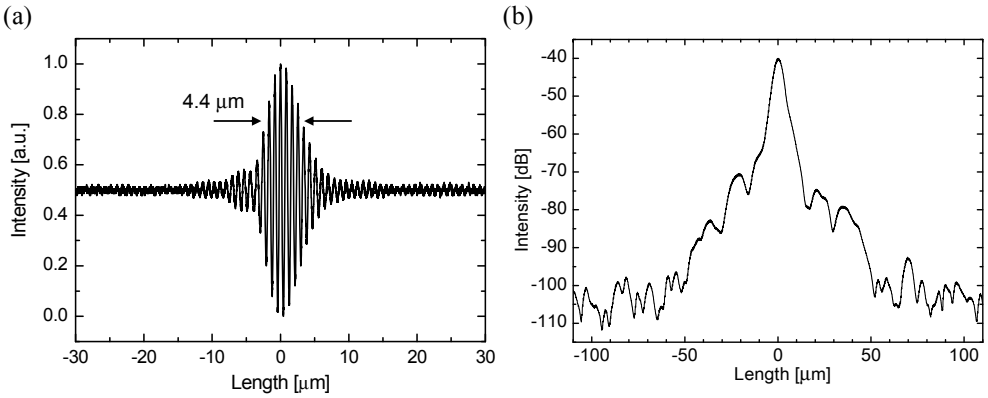

Fig. 8. (a) Interference signal of the UHR-OCT system with the developed SC source, (b) the logarithmically demodulated signal.

2.3 Characteristics of UHR-OCT systems

We compared the developed SC source, a previous one operating in the 1.7 μm wavelength region, and an SC source operating in the 1.3 μm wavelength region. The latter two were based on a fiber laser with a repetition rate of 50 MHz and an EDFA system. The configurations of these systems were described in detail in Refs. 20 and 21. The specifications of each UHR-OCT system are shown in Table 1. Although the incident power was different depending on the OCT system, the same sensitivity was achieved for the OCT system with the developed SC source at 1.7 μm wavelength and that with the SC source at 1.3 μm wavelength. In the experiment, the optical power incident on the sample surface was about 7 mW, which was below the ANSI damage threshold for skin tissue of 9.6 mW in 1.5-1.8 μm wavelength region.

Table 1. Specifications of compared UHR-OCT systems.

Light source used in OCT system	Power of the SC	Sensitivity	Axial resolution (in air)	Transverse resolution	Incident power on sample
	[mW]	[dB]	[μm]	[μm]	[mW]
Developed SC at 1.7 μm	60	105	4.4	33	6.7
Previous SC at 1.7 μm	30	95	4.6	33	3
SC at 1.3 μm	7.3	105	4.2	29	0.75

2.4 Observed samples

We imaged several biological samples with the three UHR-OCT systems mentioned above. The tested samples were a human baby tooth, a human nail, and a pig thyroid gland. A human baby tooth has an enamel layer and a dentine layer. The enamel layer contains about 4% water, and the dentine layer contains about 10% water. We chose a human baby tooth as a sample with low water absorption. A human nail mainly consists of the epidermis, dermis, nail plate, and nail bed. The epidermis and dermis contain about 58% water, and the nail

#203700 - $15.00 USD Received 24 Dec 2013; revised 15 Feb 2014; accepted 18 Feb 2014; published 26 Feb 2014

plate and nail bed contain about 15%. We chose a human nail as a sample that has both high and low water absorption properties. A pig thyroid gland was chosen as a conventional biological sample with high water-absorption and highly scattering property.

3. Results

3.1 Human baby tooth

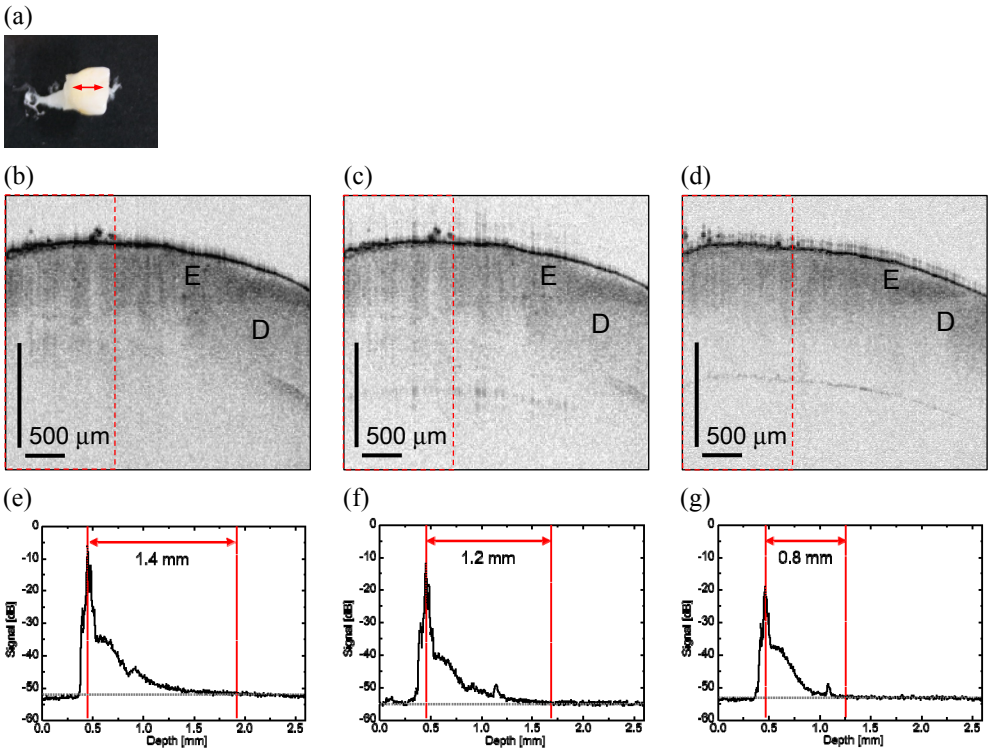

Fig. 9. (a) Photograph of the human baby tooth sample. The red arrow represents the B-scan line. (b-d) UHR-OCT images measured by (b) the developed SC source, (c) the previous one, and (d) the one at 1.3 μm wavelength region, respectively. The same gray scale was used in these three OCT images. (e-g) Depth profiles averaged over 90 A-line scans, respectively. Important features inside the sample can be distinguished, such as the enamel layer (E), and the dentin layer (D).

Figure 9(a) shows a photograph of the measured human baby tooth. In Fig. 9(a), the red arrow represents the B-scan line. Figures 9(b)–9(d) show UHR-OCT images of the human baby tooth with the developed SC source operating in the 1.7 μm wavelength region, the previously developed one, and one operating in the 1.3 μm wavelength region, respectively. The same gray scale was used in the three images. The enamel-dentine junction can be seen in all the images. Although artifacts of the tooth surface were observed at the bottom of the images in Fig. 9(c) and 9(d), it was not observed in Fig. 9(b) owing to the small sidelobe level in the interference signal for the developed SC. For quantitative analysis, we averaged 90 A-line scans from the images; the results are plotted in Figs. 9(e)–9(g). From Fig. 9(e), the highest backscattering signal was observed among the three signals. This indicates that we can perform highly sensitive UHR-OCT imaging using the developed SC source. For quantitative analysis of the penetration performance, we defined the penetration depth as the length from the top of the sample to the depth where the backscattered signal could not be distinguished from the system noise. In Figs. 9(e)–9(g), the separation between the two red

#203700 - $15.00 USD Received 24 Dec 2013; revised 15 Feb 2014; accepted 18 Feb 2014; published 26 Feb 2014

dotted lines corresponds to the penetration depth. The penetration depths were 1.4 mm, 1.2 mm, and 0.8 mm, respectively. This result indicates that a significant increase in the penetration depth was achieved with the developed SC source for the low-water-absorption samples.

3.2 Human nail

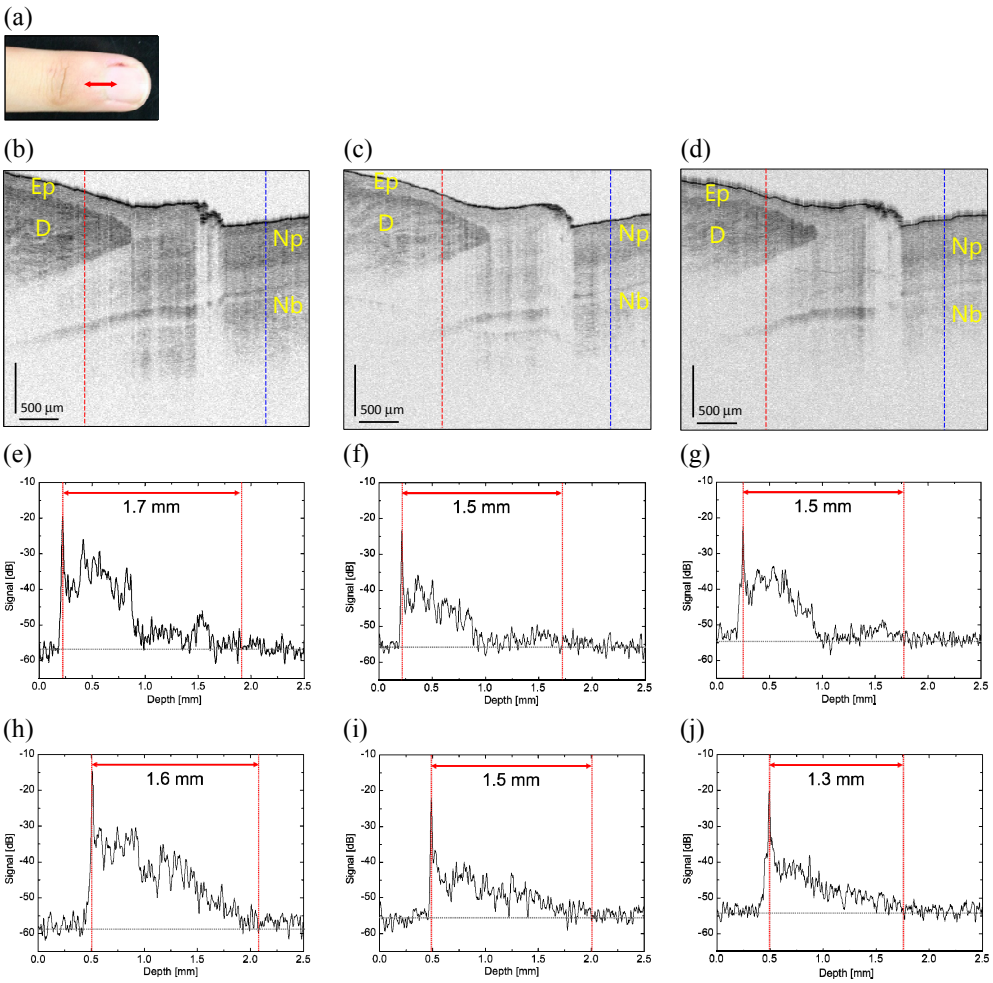

Fig. 10. (a) Photograph of the human nail sample. The red arrow represents the B-scan line. (b-d) UHR-OCT images of the sample with (b) the developed SC source, (c) the previous one, and (d) SC source at 1.3 µm wavelength region. The same gray scale was used in these three OCT images. (e-g) Depth profiles along the red dashed line in Fig. 10(b-d) at the area of epidermis and dermis. (h-j) Depth profiles along the blue dashed line in Fig. 10(b-d) at the area of nail plate and nail bed. Important features inside the sample can be distinguished, such as epidermis (Ep), dermis (D), nail plate (Np), Nail bed (Nb).

Figure 10(a) shows a photograph of the measured human nail. In Fig. 10(a), the red arrow represents the B-scan line. The same gray scale was used in the three images. We can clearly observe the biological tissues such as the epidermis, dermis, nail plate, and nail bed. The image contrast was improved by using the developed SC source. Figures 10(e)–10(g) depict depth profiles of the epidermis and dermis along the red dashed lines in Figs. 10(b)–10(d). Since the epidermis and dermis contain about 58% water, a slight improvement in penetration depth was observed using the developed SC source compared with the one

#203700 - $15.00 USD Received 24 Dec 2013; revised 15 Feb 2014; accepted 18 Feb 2014; published 26 Feb 2014

operating in the 1.3 μm wavelength region. The penetration depths were 1.7 mm, 1.5 mm, and 1.5 mm, respectively. Figures 10(h)–10(j) show the depth profile of the area of nail plate and nail bed along the blue dashed lines in Figs. 10(b)–10(d). The penetration depths were 1.6 mm, 1.5 mm, and 1.3 mm, respectively. Using the developed SC source, we confirmed that the penetration depth was improved for the low-water-absorption samples.

3.3 Pig thyroid gland

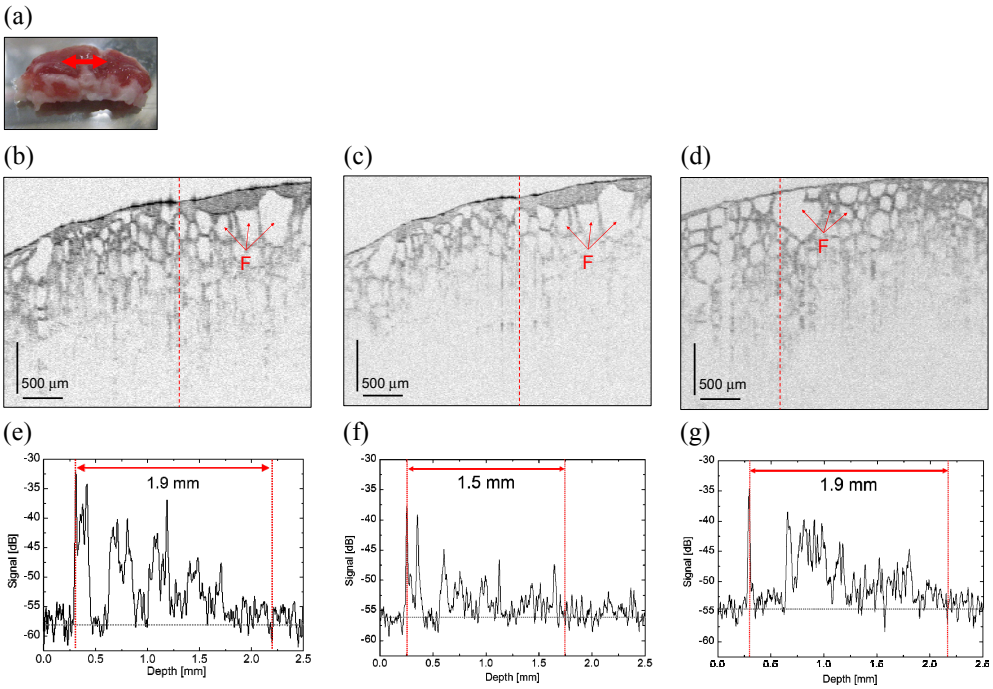

Fig. 11. (a) Photograph of the pig thyroid gland sample. (b-d) UHR-OCT images of the sample with (b) the developed SC source, (c) the previous one, and (d) SC source at 1.3 μm wavelength region. The same gray scale was used in these three OCT images. (e-g) Depth profiles along the red dashed line in Fig. 11(b-d). (F): follicle.

Figure 11(a) shows a photograph of the measured pig thyroid gland. Figures 11(b), 11(c) show *in vitro* UHR-OCT images of the sample. The same gray scale was used in the three images. The microstructure, such as follicles in the thyroid gland, was visualized. Figures 11(e)–11(g) depict depth profiles along the red dashed lines in Figs. 11(b)–11(d). The penetration depths were 1.9 mm, 1.5 mm, and 1.9 mm, respectively. Owing to the water absorption, a clear improvement in penetration was not confirmed by using the developed SC source compared with the SC source operating in the 1.3 μm wavelength region. However, an improvement in sensitivity was confirmed owing to the higher average power of the SC. Compared with the previous SC source operating in the 1.7 μm wavelength region, both the sensitivity and the penetration depth were improved by using the developed SC source.

Figures 12(a) and 12(b) show *en-face* images of the thyroid gland at the same depth of 0.58 mm from the surface, obtained with the developed SC source and the previously developed one. The same gray scale was used in both *en-face* images. The image contrast obtained with the developed SC source was much higher than that obtained with the previous one. This result shows that the developed SC source allows us to perform highly penetrative UHR-OCT.

#203700 - $15.00 USD Received 24 Dec 2013; revised 15 Feb 2014; accepted 18 Feb 2014; published 26 Feb 2014

Figure 12(c) shows a reconstructed 3D image of the pig thyroid gland obtained with the developed SC source. In the 3D image shown in Media 1, the three-dimensional structure of a follicle was observed clearly by using the developed SC source.

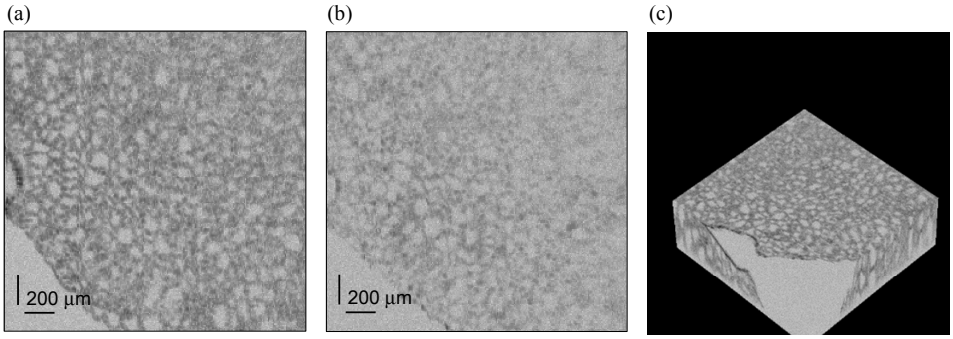

Fig. 12. (a,b) *En-face* images of the pig thyroid gland at the same depth of 0.58 mm from the surface measured by (a) the developed SC source and (b) the previous SC source. The same gray scale was used in both images. (c) 3D image of the pig thyroid gland measured by the developed SC source (Media 1).

4. Conclusion

We have developed a high-power supercontinuum (SC) source operating in the 1.7 μm wavelength region to demonstrate highly penetrative ultrahigh-resolution optical coherence tomography (UHR-OCT). Using a polyimide film containing dispersed single-wall carbon nanotubes, we constructed a soliton mode-locked fiber laser with a high repetition rate of 110 MHz. Based on this fiber laser, we built a high-power SC source operating in the 1.7 μm wavelength region with a maximum output power of 60 mW. The developed light source consisted almost entirely of all-fiber devices, and it can be used as a compact, stable, and practical light source. By using the developed SC source, a sensitivity of 105 dB was achieved in the UHR-OCT system, which was 10 dB higher than that of the previous one. The further improvement of sensitivity is expected by increasing the output power of SC source. An axial resolution of 3.2 μm was achieved in biological tissue with the developed SC source. We compared UHR-OCT images of some biological tissue samples, measured with the developed SC source, a previously developed one, and a SC source operating in the 1.3 μm wavelength region. By using the developed SC source, we were able to perform highly sensitive and penetrative UHR-OCT imaging of low-water-absorption samples.

#203700 - $15.00 USD Received 24 Dec 2013; revised 15 Feb 2014; accepted 18 Feb 2014; published 26 Feb 2014